Interferometric Alignment of the X-SAR Antenna System on the Space Shuttle Radar Topography Mission

Dirk Geudtner, Manfred Zink, Christoph Gierull, *Member, IEEE*, and Scott Shaffer

Abstract—The on-orbit alignment of the antenna beams of both the X-band and C-band radar systems during operations of the shuttle radar topography mission/X-band synthetic aperture radar (SRTM/X-SAR) was a key requirement for achieving best interferometric performance. In this paper, we consider the X-SAR antenna beam alignment in azimuth. For a single-pass cross-track SAR interferometer, we establish the relation between yaw and pitch misalignment of the antenna beams and the resulting relative shift of the Doppler frequency bands. This relation is used to provide solutions for the mechanical adjustments of the outboard antenna and electronic beam steering to correct for azimuth misalignment. Furthermore, the effects of the X-SAR effective outboard antenna pattern on the azimuth beam alignment are analyzed. As a result, a so-called "relaxing" factor is derived, which increases the limit for the difference in antenna azimuth angle with respect to the requirement on spectral overlap, and hence spatial interferogram resolution. However, we also show that the alignment requirement is driven by the constraint on decreasing the azimuth ambiguity-to-signal ratio (AASR) for the effective outboard antenna pattern to reduce the resulting additional height error. The strategy for misalignment determination and correction is presented, and results of the analysis of the in-flight X-SAR antenna beam alignment are discussed.

Index Terms—SAR antenna beam alignment, SAR interferometry, shuttle radar topography mission/X-band synthetic aperture radar (SRTM/X-SAR).

I. INTRODUCTION

THE shuttle radar topography mission/X-band synthetic aperture radar (SRTM/X-SAR) was the first spaceborne single-pass SAR interferometry mission. The objective was to generate three-dimensional digital terrain maps of the entire earth's landmass between 60° North and 57° South latitude during an 11-day space shuttle flight in February 2000. SRTM/X-SAR was a cooperative project of NASA, the National Imagery and Mapping Agency (NIMA), the German Aerospace Center (DLR), and the Italian Space Agency (ASI).

SRTM/X-SAR comprised two interferometric radar systems: 1) the C-band SAR (C-RADAR) and 2) the X-band SAR (X-SAR). These are modified versions of the spaceborne imaging radar-C (SIR-C) and X-band SAR (X-SAR) that were flown aboard two space shuttle missions in April and October 1994 [1], [2]. During these previous missions, some repeat-pass interferometric data pairs were acquired with a time separation of six months between the first and second flight, and one day during the last three days of the October flight [3], respectively.

For SRTM/X-SAR, both SIR-C and X-SAR were modified to operate as cross-track fixed-baseline interferometers. The C-RADAR used a dual polarization ScanSAR mode to achieve a swath width of 250 km and allows continuous coverage. The X-SAR system operated in a high-resolution strip-map mode with a swath width of 50 km. Each radar instrument consisted of an "inboard" transmit/receive radar antenna (primary channel) located in the payload bay and an "outboard" receive-only antenna (secondary channel). Both outboard antennas were mounted on an outboard support structure (OSS) that was located at the end of a 60 m deployable/retractable mast forming the interferometric baseline.

This single-pass SAR interferometer configuration enables the removal of large error sources inherent with the repeat-pass technique, such as baseline uncertainties, temporal decorrelation effects, and atmospheric inhomogeneities. However, a key requirement for achieving best interferometric performance is that the pointing of the outboard antenna beam coincides with the inboard antenna beam. Beam misalignment reduces the overlap between the antenna footprints and degrades the signal-to-noise ratio (SNR) in the secondary channel, thus decreasing the interferometric signal correlation. The phase noise in the interferograms may also increase as result of a high azimuth ambiguity-to-signal ratio (AASR), and a relative shift of the inboard and outboard Doppler frequency bands due to different squint angles, causing a reduction in azimuth spectral overlap.

In this paper, we concentrate on the on-orbit X-SAR antenna beam alignment. We consider the relation between pitch and yaw displacements of the outboard antenna and the resulting relative shift of the Doppler frequency bands to derive solutions for the antenna beam alignment in azimuth. Then, we analyze the effects of the antenna patterns on the alignment, considering the specific X-SAR requirements on spatial resolution and height accuracy. Finally, results of the in-flight X-SAR antenna beam alignment obtained during the mission are discussed.

The alignment of the antenna beams on SRTM/X-SAR, respective for the C-RADAR and X-SAR system, differs because of the long mast structure from those of airborne single-pass SAR interferometer configurations. It was expected that the relative beam alignment between the inboard and outboard antenna of each radar system on SRTM/X-SAR could be affected by several factors: Gravity effects, pre-flight assembly and alignment errors, launch shifts [4], and a small discrepancy between the mechanical and electrical antenna boresight result in a quasistatic pointing bias. In-flight thermal distortions and shuttle-induced disturbances due to attitude hold (thruster firings) and crew motion could also cause dynamic mast twisting and bending effects. Both static and dynamic effects needed to be measured and compensated to align the electrical boresights of the inboard and outboard antenna of each radar system to a very tight tolerance. In support of this task, additional instruments and equipment were added to SRTM/X-SAR. This included the attitude and orbit determination avionics (AODA), the mechanical adjustment structure called "milkstool," and the beam auto tracker (BAT).

The AODA system is a suite of sensors that provided in-flight measurements to verify mast deployment and to support antenna alignment. A detailed description of the AODA instruments and their functions is given in [5]. Throughout the mission, AODA measured and monitored the outboard to inboard antenna mechanical alignment in pitch, yaw, and roll. It further provided the orbital state vectors, the time-base for both radar systems, and updated measurements that are used in the post-processing to reconstruct the mechanical baseline vector.

The milkstool, located at the mast tip, is a two-axis actuator for the OSS to mechanically adjust the outboard antennas of both radar systems. The milkstool provided up to $\pm 4°$ pitch and $\pm 2.8°$ yaw steering capability, and was steered by the shuttle crew using AODA onboard alignment solutions.

The C-RADAR BAT is an electronic assembly to steer the azimuth outboard antenna beam. It enabled a real-time monitoring of the along-track antenna electrical alignment for each C-RADAR subswath and could automatically compensate for up to $\pm 0.3°$ dynamic misalignment. X-SAR was designed to use the C-RADAR BAT signals as input for its semi-automatic X-SAR BAT system. However, as it turned out during the mission, use of the BAT system was not required due to only small dynamic beam misalignment effects.

For measuring and monitoring the in-flight mechanical antenna alignment by the AODA system and for determination of the required milkstool rotations, two coordinate systems were introduced: the inboard coordinate system (ICS), and the outboard coordinate system (OCS). The origin of the ICS is referenced to the AODA sensor plate that is located on the C-RADAR inboard antenna. The origin of the OCS is located on the flip hinge of the OSS. Details of these coordinate systems are depicted in Fig. 1. Note that the ICS and OCS Z-axes are normal to the radiating surface of the inboard antenna and outboard antenna, respectively. In the following sections, the coordinate axes of ICS and OCS are considered to be unit vectors.

A. X-SAR Antenna System

The X-SAR inboard antenna with a length of 12 m had an azimuth and elevation beamwidth of $0.14°$ and $5.5°$,

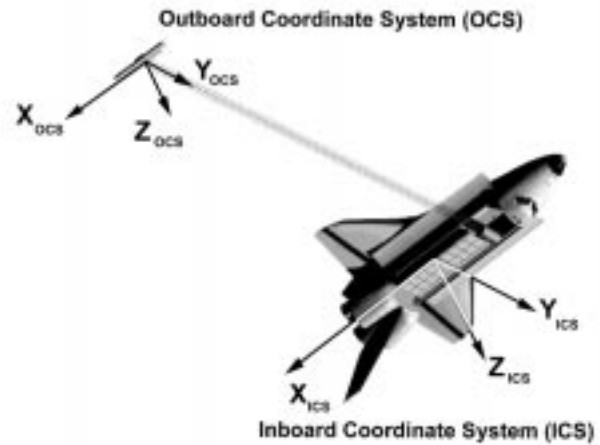
Fig. 1. SRTM/X-SAR inboard and outboard coordinate systems During mapping operations the ICS and OCS Y-axes were rotated by 45° relative to the loacl horizontal plane.

TABLE I
X-SAR KEY SYSTEM PARAMETERS

Wavelength	0.03122 m
Chirp bandwidth	9.5 MHz
Pulse repetition frequency (PRF)	1674 Hz
Processed bandwidth in azimuth (PBW)	1180 Hz
Look angle (swath center)	$52°$
Swath width	50 km
Slant range (mid swath)	400 km
X-SAR baseline (nominal)	60.96 m
Baseline tilt angle (nominal)	$45°$
Inboard antenna length	12 m
Outboard antenna length	6 m
Inboard antenna beamwidth in azimuth	$0.14°$
Outboard antenna beamwidth in azimuth	$0.28°$
Inboard antenna beamwidth in elevation	$5.5°$
Outboard antenna beamwidth in elevation	$5.5°$

respectively. Its tri-drive tilt mechanism pointed the antenna in elevation to $-7°$ relative to the C-RADAR midswath. This placed the X-SAR swath between the third and fourth C-RADAR ScanSAR subswath. The X-SAR elevation angle range is between $-4.5°$ and $-9.5°$, which is equivalent to a look angle range between $49.5°$ and $54.5°$. Unlike the C-RADAR inboard antenna, the X-SAR primary antenna had no azimuth beam steering capability. In contrast, the 6-m long X-SAR outboard antenna with an azimuth beamwidth of $0.28°$ provided an electronic beam steering capability in azimuth of $\pm 0.9°$ with an approximate step size of $0.025°$. However, simulations indicated that the electronic beam steering should be limited to within $\pm 0.5°$, since otherwise the resulting outboard antenna pattern would become increasingly distorted. X-SAR key system parameters are summarized in Table I. A detailed description of the X-SAR instrument can be found elsewhere [6].
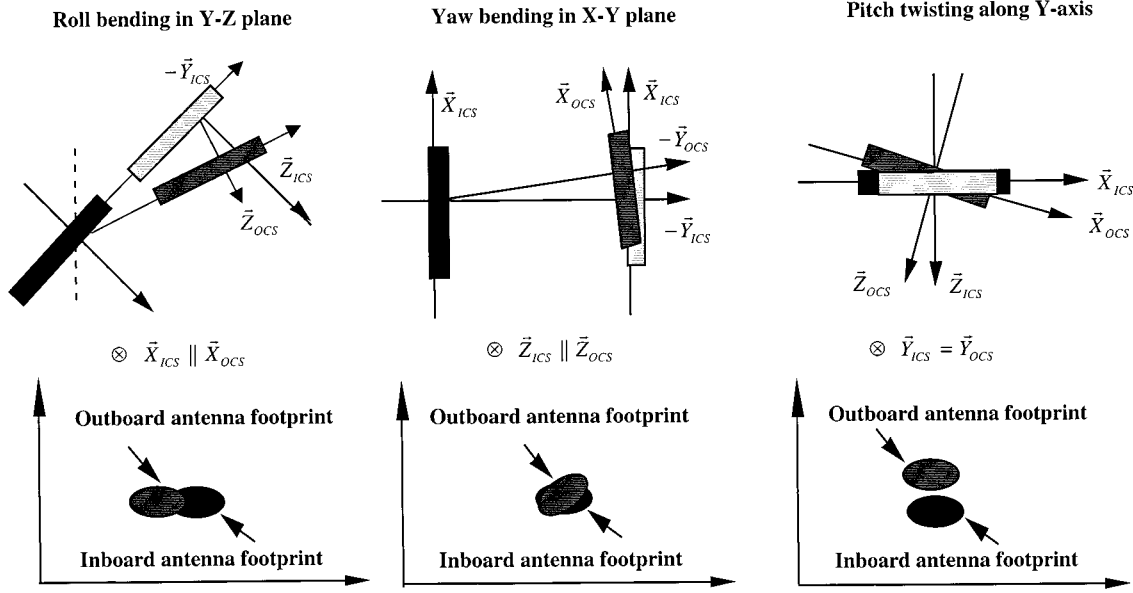
Fig. 2.   Illustration of roll, yaw, and pitch rotations of the OCS with respect to the ICS, and the resulting effects on antenna footprint overlap.

B. Concept for Antenna Beam Alignment

The on-orbit antenna beam alignment was based on a combination of AODA and Doppler centroid frequency, and initially also BAT, measurements along with mechanical adjustments and electronic antenna beam steering for correction of misalignment. The basic concept was that after mast deployment, the AODA system provides estimates of the initial antenna mechanical misalignment in roll, pitch, and yaw. For the X-SAR system, a roll misalignment could be compensated by a mechanical rotation in elevation of the inboard antenna. The AODA pitch and yaw estimates would provide solutions for a "coarse" milkstool adjustment. This minimizes the quasistatic pointing bias in azimuth to a level where the inboard and outboard antenna beams of each radar system overlap sufficiently, enabling a measurement of the antenna electrical boresight alignment by means of a Doppler frequency analysis of down linked two-channel C-RADAR and X-SAR data. Note that in contrast to the limited radar data downlink capability, the AODA system provided continuous measurements of the mechanical antenna alignment. However, these measurements were expected to be biased with respect to the electrical boresight alignment due to systematic instrument errors and mechanical location errors resulting from pre-launch surveying inaccuracies and launch-induced shifts. Therefore, Doppler frequency measurements are used to determine the mechanical/electrical bias in the AODA pitch and yaw estimates. Then, the calibrated AODA estimates provide the solution for a "fine" adjustment of the milkstool. The alignment is verified by additional Doppler frequency measurements. A possible residual error in the azimuth beam alignment could be compensated by electronic antenna beam steering.

It should be noted that a milkstool rotation steered simultaneously both C-RADAR and X-SAR outboard antennas in the same direction and by the same amount. Therefore, estimation of the appropriate adjustments required consideration of the Doppler frequency analysis results from both radar systems. However, the two radar instruments provided separate electronic beam steering capabilities to compensate for residual misalignment. Also, a possible offset between the electrical boresights of the C-RADAR and X-SAR antennas had to be considered in the alignment determination. Hence, an independent electrical beam alignment estimation and verification was required that considered the specifics of the respective radar systems.

II. MISALIGNMENT EFFECTS

As a result of the static antenna beam pointing offset and dynamic mast twisting in pitch, and bending effects in yaw and roll, the OCS is rotated relatively to the ICS. Fig. 2 illustrates the resulting reduction in the overlap between inboard and outboard antenna footprints in along-track and cross-track directions, respectively. For the X-SAR system, the alignment is relatively insensitive to small changes in the roll angle of the outboard antenna due to the large antenna beamwidth in elevation. Also, as usual for spaceborne SAR interferometers, we assume parallel beam paths since the slant range is significantly larger than the baseline. Hence, a possible reduction in the cross-track antenna footprint overlap due to baseline is negligible. Since the alignment sensitivity in azimuth is an order of magnitude higher than in range, we concentrate in the following on the antenna beam alignment in azimuth. Here, we briefly review the effects of beam misalignment on the interferometric phase noise. Specifically, we consider the SNR, the relative shift of Doppler frequency bands, and the AASR. In Section IV, these effects are further discussed with respect to the specific requirements on the azimuth beam alignment of the X-SAR antenna system. The implication of misalignment-induced phase noise on the height accuracy can be assessed by evaluating the following expression [7]:

$$\sigma_h = \frac{\lambda R \sin\theta}{2\pi B \cos(\theta - \xi)} \sigma_\phi \qquad (1)$$

where
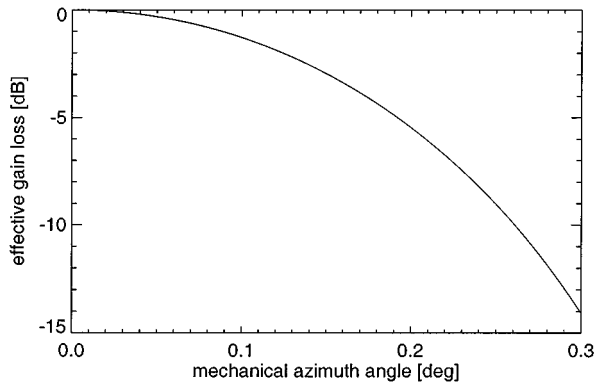
R slant range;

B baseline;

Fig. 3.   Effective antenna gain loss in the secondary channel due to azimuth misalignment.
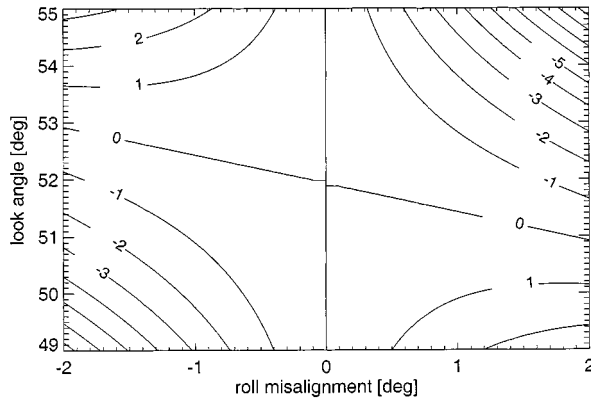

Fig. 4.   Contour plot of the effective gain change in the secondary channel across the X-SAR swath due to roll misalignment.

θ look angle;
ϕ interferometric phase;
ξ baseline tilt angle;
λ wavelength.

Equation (1) is modified for a SAR interferometer configuration with one transmit/receive antenna and one receive-only antenna. Using X-SAR parameters (see Table I), a phase standard deviation of $\sigma_\phi = 1°$ causes a height standard deviation of $\sigma_h = 0.45$ m.

A. Signal-to-Noise Ratio (SNR)

The reduced overlap of antenna footprints causes a gain loss in the secondary channel, decreasing the SNR in this channel, and hence the inferred signal correlation [8]. Fig. 3 shows the effective gain loss in the secondary X-SAR channel due to azimuth misalignment. For comparison, the contour plot in Fig. 4 shows the effective gain change due to roll misalignment across the X-SAR swath. Whereas an azimuth misalignment leads to an overall gain reduction, roll misalignment is less critical as it only reduces the gain in near or far ranges.

B. Relative Shift of Doppler Frequency Bands

The relative pitch and yaw displacements between inboard and outboard antennae cause a relative shift of the corresponding Doppler frequency bands by Δf_{DC}, decreasing the inferred signal correlation [9]. Thus, a key requirement for achieving signal correlation in azimuth is that $|\Delta f_{DC}|$ must

not exceed the processed azimuth bandwidth (*PBW*), which is the theoretical upper limit (i.e., for X-SAR: $PBW = 1180$ Hz). However, the nonoverlapping parts of the Doppler spectra increase the phase noise in the interferogram, and hence the height error. For example, a $|\Delta f_{DC}| = 100$ Hz would lead to a decorrelation of $|\Delta f_{DC}|/PBW = 0.085$ [9]. Using the relation between phase noise and interferometric correlation [7], [9], for a one-look X-SAR interferogram, this is equivalent to a phase standard deviation of about $\sigma_\phi = 18°$ causing a height error of about $\sigma_h = 8.1$ m. To suppress this height error contribution, it is common practice to reduce the phase noise by an azimuth bandpass filtering [10] or by processing both channels with the mean of the two Doppler centroid frequencies. However, this improvement is at the expense of a reduced spatial resolution due to the reduction in the interferogram azimuth bandwidth. Considering the specified interferometric four-look (in azimuth) spatial resolution of 30 m for the X-SAR digital elevation model (DEM) [11], the requirement on the maximum allowable relative shift in Doppler frequency bands was that: $|\Delta f_{DC}^{\max}| = PBW/4 \cong 300$ Hz.

C. Azimuth Ambiguity-to-Signal Ratio (AASR)

The antenna beam misalignment also causes an increase in the AASR. Azimuth ambiguities arise from aliasing effects due to the finite sampling of the azimuth frequency spectrum at the pulse repetition frequency (PRF) [12]. In accordance with the results from coherent error statistics [13], for an AASR of less than -10 dB the resulting phase standard deviation can be approximately calculated [14] as

$$\sigma_\phi = \frac{\arctan(RASR)}{\sqrt{2}} \qquad (2)$$

where $RASR$ is given to

$$RASR = \frac{1}{\frac{1}{\text{AASR}^I} + \frac{1}{\text{AASR}^O}}$$

where AASR^I and AASR^O are the inboard and outboard AASR's, respectively.

III. GEOMETRICAL CONSIDERATIONS

In this section, we expand the known relation between SAR antenna attitude variations (primarily spacecraft attitude) and a Doppler centroid frequency shift that was previously derived for a single antenna SAR system only [15], [16], for a SAR interferometer configuration with one transmit/receive and one receive-only antenna. This relates the pitch and yaw displacements of the outboard antenna to the relative shift of the inboard and outboard Doppler frequency bands. Based on this relation, the mechanical/electrical bias in the AODA alignment estimates is determined from Doppler frequency measurements, and hence the "fine" adjustment rotations of the milkstool for correction of the static antenna beam pointing offset. Also, we establish the relationship between the squint angle difference (i.e., between inboard and outboard electrical boresight) and the resulting difference in the antenna azimuth angle. This angle is used for electronic beam steering of the X-SAR outboard antenna to compensate for residual misalignment.
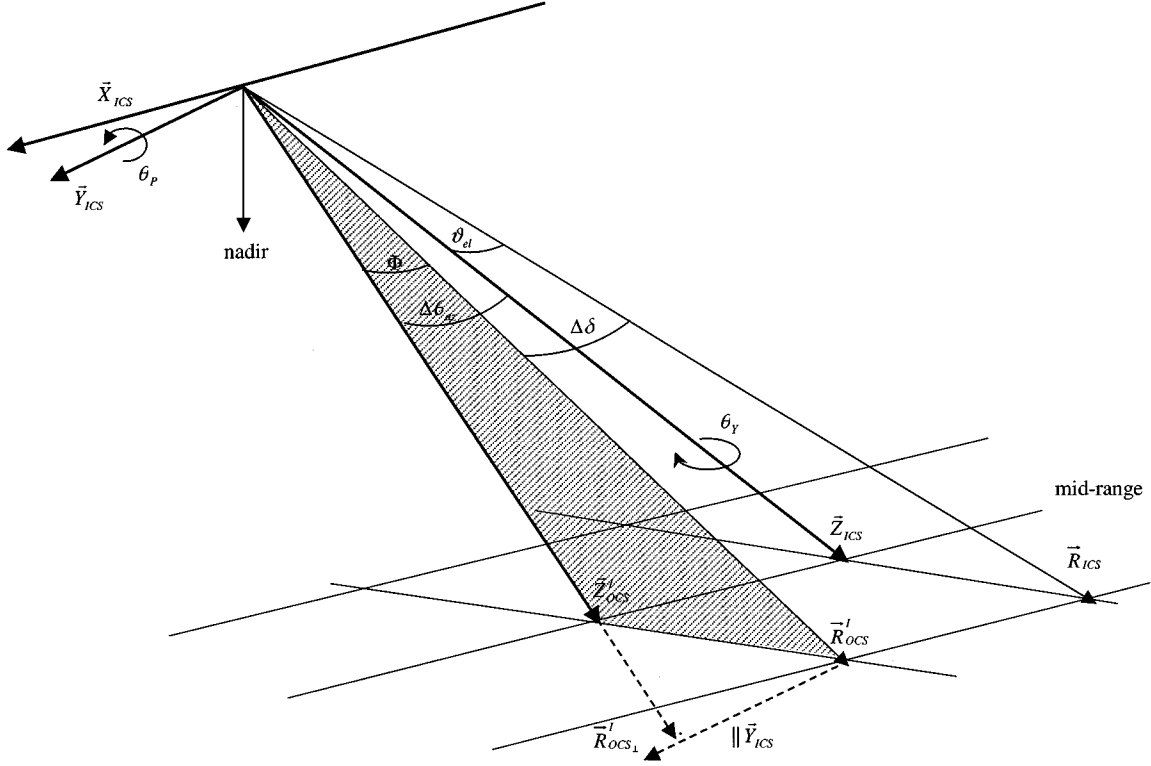
Fig. 5.   Illustration of pitch and yaw mast rotation effects on the X-SAR antenna beam geometry. The hatched area represents the boresight elevation plane of the outboard antenna transformed to the ICS. $\vec{Z}_{ICS}$ and $\vec{Z}_{OCS}^{I}$ are the antenna normal vectors in the ICS. $\vec{R}_{ICS}$ and $\vec{R}_{OCS}^{I}$ are arbitrary pointing vectors in the ICS.

The requirement for an antenna beam alignment is that the normal vector of the outboard antenna $\vec{Z}_{OCS}$ coincides with the normal vector of the inboard antenna $\vec{Z}_{ICS}$ (see Figs. 2 and 5). Assuming that the antenna beams are aligned in elevation, azimuth alignment is sufficient when the actual Doppler plane (i.e., electrical boresight) of the outboard antenna coincides with the actual Doppler plane of the inboard antenna. In other words, the beams are completely aligned when the difference between inboard and outboard squint angles, δ^{I} and δ^{O}, respectively, is $\Delta\delta = \delta^{I} - \delta^{O} = 0$. The squint angle is the angle between the zero-Doppler plane and the antenna electrical boresight, respective for the inboard and outboard antenna. For SRTM/X-SAR, δ^{I} and δ^{O} are defined as positive in the direction of the velocity vector, which means toward the aft end of the shuttle since it is flying tail forward during mapping operations.

A. Determination of Pitch and Yaw Rotations

The Doppler centroid frequency of the inboard channel can be expressed [15] as

$$f_{DC}^{I} = \frac{2}{\lambda}\frac{\vec{v}\vec{R}_{ICS}(\vartheta_{el})}{\left|\vec{R}_{ICS}(\vartheta_{el})\right|} = \frac{2}{\lambda}|\vec{v}|\sin\delta^{I} \qquad (3)$$

where $\vec{R}_{ICS}(\vartheta_{el})$ is an arbitrary pointing vector of the inboard antenna at an elevation angle ϑ_{el} within the swath given in ICS coordinates. The elevation angle ϑ_{el} is the angle between the mechanical boresight of C-RADAR and the electrical boresight along the narrow axis of the antenna. ϑ_{el} is defined as positive

toward nadir. $\vec{v}$ is the shuttle's velocity in WGS-84 coordinates with $|\vec{v}| \cong 7.5$ km s^{-1}, and λ is the wavelength.

In the case of a misalignment between the electrical boresight of the inboard and outboard antenna, causing a squint angle difference $\Delta\delta$, the Doppler centroid frequency of the outboard channel can be written as

$$
\begin{aligned}
f_{DC}^{O} &= \frac{2}{\lambda}\frac{\vec{v}\vec{R}_{OCS}(\vartheta_{el})}{\left|\vec{R}_{OCS}(\vartheta_{el})\right|} = \frac{2}{\lambda}|\vec{v}|\sin\delta^{O} \\
&= \frac{2}{\lambda}|\vec{v}|\sin(\delta^{I} + \Delta\delta) \\
&= \frac{2}{\lambda}|\vec{v}|(\sin\delta^{I}\cos\Delta\delta + \cos\delta^{I}\sin\Delta\delta) \\
&\cong f_{DC}^{I} + \frac{2}{\lambda}|\vec{v}|\cos\delta^{I}\sin\Delta\delta \qquad (4)
\end{aligned}
$$

with $\cos\Delta\delta \approx 1$, for a small squint angle difference. Here, $\vec{R}_{OCS}(\vartheta_{el})$ is an arbitrary pointing vector of the outboard antenna at an elevation angle ϑ_{el} within the swath given in OCS coordinates. Then, the difference between inboard and outboard Doppler frequencies is related to the difference in the corresponding squint angles as

$$\Delta f_{DC} = f_{DC}^{I} - f_{DC}^{O} = \frac{2}{\lambda}|\vec{v}|\cos\delta^{I}\sin\Delta\delta. \qquad (5)$$

For a sufficient zero-Doppler steering of the shuttle, the squint angle of the inboard antenna is so small that $\cos\delta^{I} \approx 1$. Otherwise, the inboard squint angle can be expressed from (3) as

$\cos \delta^I = \sqrt{1 - (\lambda f_{DC}^I / 2|\vec{v}|)^2}$, and would then need to be considered in (5). Note that during SRTM/X-SAR mapping operations, the shuttle's attitude was kept within a narrow zero-Doppler deadband, which was nominally $\pm 0.1°$, and then relaxed to $\pm 0.2°$ during the mission.

We now express the squint angle difference as a function of pitch and yaw outboard antenna displacements. The pitch and yaw angles, θ_P and θ_Y, respectively, describe the rotation of the outboard antenna relative to the inboard antenna about the ICS Y-axis and the ICS Z-axis, respectively (see Figs. 2 and 5). Both are defined as positive when the outboard antenna is pointed more toward the shuttle tail than the inboard antenna. Referring to Fig. 5, in each coordinate system we consider at the same elevation angle (i.e., assuming alignment in elevation) an arbitrary pointing vector, which is defined as

$$\vec{R}_{ICS}(\vartheta_{el}) = \{0, R_{ICS} \sin \vartheta_{el}, R_{ICS} \cos \vartheta_{el}\}$$

and

$$\vec{R}_{OCS}(\vartheta_{el}) = \{0, R_{OCS} \sin \vartheta_{el}, R_{OCS} \cos \vartheta_{el}\}$$

respectively, where R_{ICS} and R_{OCS} are the corresponding slant range distances. Note that for simplicity, we assume exact zero-Doppler conditions for the inboard channel, implying that $\delta^I = 0$, and hence the X-component of $\vec{R}_{ICS}$ in the ICS is zero. Furthermore, we assume that the electrical boresight of the outboard antenna is aligned with the Z-axis of the OCS. That means the X-component of $\vec{R}_{OCS}$ in the OCS is also zero. To account for the pitch and yaw rotations, $\vec{R}_{OCS}$ is transformed from the OCS to the ICS, i.e., $\vec{R}_{OCS}^I(\vartheta_{el}) = T_P T_Y \vec{R}_{OCS}(\vartheta_{el})$, with

$$\vec{R}_{OCS}^I(\vartheta_{el})$$
$$= \begin{bmatrix} \cos \theta_P & 0 & \sin \theta_P \\ 0 & 1 & 0 \\ -\sin \theta_P & 0 & \cos \theta_P \end{bmatrix} \begin{bmatrix} \cos \theta_Y & -\sin \theta_Y & 0 \\ \sin \theta_Y & \cos \theta_Y & 0 \\ 0 & 0 & 1 \end{bmatrix}$$
$$\cdot \begin{bmatrix} 0 \\ R_{OCS} \sin \vartheta_{el} \\ R_{OCS} \cos \vartheta_{el} \end{bmatrix}$$
$$= R_{OCS} \begin{bmatrix} -\sin \vartheta_{el} \sin \theta_Y \cos \theta_P + \sin \theta_P \cos \vartheta_{el} \\ \sin \vartheta_{el} \cos \theta_Y \\ \sin \vartheta_{el} \sin \theta_Y \sin \theta_P + \cos \vartheta_{el} \cos \theta_P \end{bmatrix} \quad (6)$$

where T_P and T_Y denote the rotation matrices in pitch and yaw, respectively. Assuming very small rotation angles, i.e., $\cos \theta_i \approx 1$, $\sin \theta_i \approx \theta_i$, and $\theta_i \theta_j \approx 0$ for $i, j \in \{P, Y\}$, then the outboard pointing vector can be approximated in ICS coordinates as

$$\vec{R}_{OCS}^I(\vartheta_{el}) \cong R_{OCS} \begin{bmatrix} \theta_P \cos \vartheta_{el} - \theta_Y \sin \vartheta_{el} \\ \sin \vartheta_{el} \\ \cos \vartheta_{el} \end{bmatrix}. \quad (7)$$

Equation (7) shows that the transformed and normalized outboard pointing vector $\vec{R}_{OCS}^I / \|\vec{R}_{OCS}^I\|$ differs only in the

X-component from $\vec{R}_{ICS} / \|\vec{R}_{ICS}\|$. The resulting squint angle difference is then given as

$$\sin \Delta \delta = \theta_P \cos \vartheta_{el} - \theta_Y \sin \vartheta_{el} \quad (8)$$

where $\Delta \delta$ is measured at a given ϑ_{el} between $\vec{R}_{ICS}(\vartheta_{el})$ and $\vec{R}_{OCS}^I(\vartheta_{el})$ (see Fig. 5).

B. Determination of Antenna Azimuth Angle

We now relate the squint angle difference $\Delta \delta$ to the difference between inboard and outboard antenna azimuth angle $\Delta \theta_{az}$. The azimuth angle θ_{az} is the angle between the mechanical and electrical boresight in the azimuth antenna plane, and describes the actual antenna beam steering direction. It is defined as positive pointing toward the shuttle nose. In the X-SAR case only the outboard antenna can be steered in azimuth either by a mechanical milkstool rotation in pitch and yaw or by an equivalent electronic beam steering. Henceforth, $\Delta \theta_{az}$ represents the change in the beam steering direction of the X-SAR outboard antenna relative to the X-SAR inboard antenna beam. As illustrated in Fig. 5, $\Delta \theta_{az}$ can be expressed as

$$\sin \Delta \theta_{az} = \cos(\pi/2 - \theta_{az}) = \frac{\vec{v}}{|\vec{v}|} \vec{Z}_{OCS}^I$$
$$= \frac{\vec{v} \cdot \vec{R}_{OCS_\perp}^I}{|\vec{v}| \left| \vec{R}_{OCS_\perp}^I \right|} \quad (9)$$

where $\vec{R}_{OCS_\perp}^I$ is the projection of $\vec{R}_{OCS}^I$ onto $\vec{Z}_{OCS}^I$, which is $\vec{Z}_{OCS}$ transformed to the ICS. $\Delta \theta_{az}$ lies in the plane defined by the normal vectors of the inboard and outboard antenna, $\vec{Z}_{ICS}$ and $\vec{Z}_{OCS}^I$, respectively, and the ICS origin. Furthermore, from Fig. 5, we can express the squint angle difference as

$$\sin \Delta \delta = \cos(\pi/2 - \Delta \delta) = \frac{\vec{v} \cdot \vec{R}_{OCS}^I}{|\vec{v}| \left| \vec{R}_{OCS}^I \right|}$$
$$= \frac{\vec{v} \cdot \left(\vec{R}_{OCS_\perp}^I + \mu \vec{Y}_{ICS} \right)}{|\vec{v}| \left| \vec{R}_{OCS}^I \right|} \quad \text{for } \mu \in \Re \quad (10)$$

where μ is the Y-component of $\vec{R}_{OCS}^I$.

Taking into account that the vectors $\vec{v}$ and $\vec{Y}_{ICS}$ are orthogonal and that $\cos \Phi = |\vec{R}_{OCS_\perp}^I| / |\vec{R}_{OCS}^I|$, and inserting (9) into (10) yields

$$\sin \Delta \delta = \frac{\vec{v} \cdot \vec{R}_{OCS_\perp}^I}{|\vec{v}| \left| \vec{R}_{OCS_\perp}^I \right|} \cos \Phi = \sin \Delta \theta_{az} \cos \Phi. \quad (11)$$

Substituting (8) into (11), and also assuming that $\Phi \cong \vartheta_{el}$ for small θ_P and θ_Y, yields

$$\sin \Delta \theta_{az} \cos \vartheta_{el} \cong \sin \Delta \delta = \theta_P \cos \vartheta_{el} - \theta_Y \sin \vartheta_{el} \quad (12)$$

which can be approximated for small $\Delta \theta_{az}$ as

$$\Delta \theta_{az} \cong \theta_P - \theta_Y \tan \vartheta_{el}. \quad (13)$$
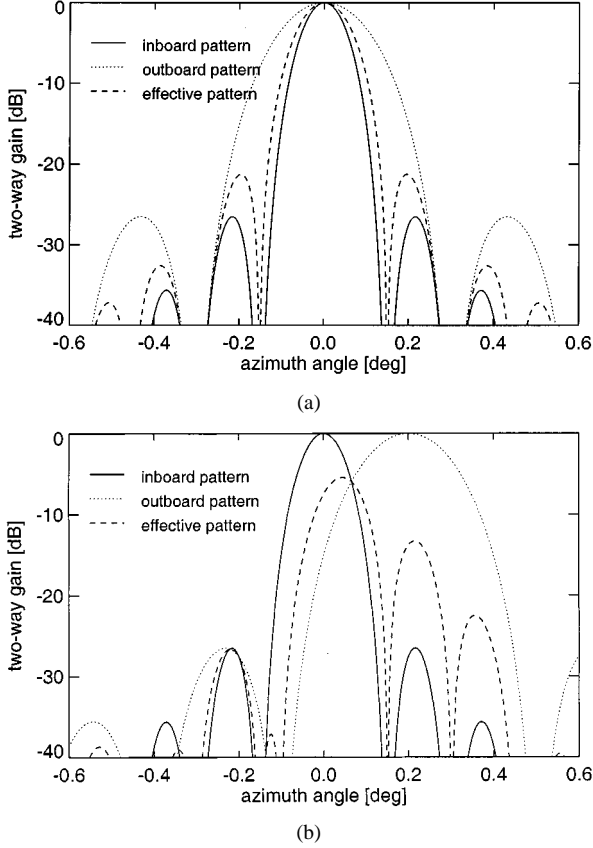
(a)

(b)

Fig. 6. (a) X-SAR inboard and outboard antenna pattern, and the resulting two-way effective pattern of the outboard antenna for an exact azimuth beam alignment. (b) X-SAR inboard and outboard antenna pattern, and the resulting two-way effective pattern of the outboard antenna for an azimuth beam misalignment of 0.2°.

Evaluating (13), we can see that the relative change in antenna azimuth angle is dominated by the pitch-induced rotation. For example, for the C-RADAR midswath, where $\vartheta_{el} = 0°$, it follows that $\Delta\theta_{az} \cong \theta_P$.

IV. EFFECTS OF AZIMUTH ANTENNA PATTERN

Accurate estimation of the mechanical milkstool adjustments and the equivalent azimuth beam steering angle from Doppler centroid frequency measurements requires consideration of the two different radiation patterns of the inboard and outboard antenna. The outboard antenna is receive-only, and as a result its effective pattern is the superposition of the one-way diagrams of both inboard and outboard antenna. Thereby, the effective outboard pattern in azimuth is governed by the narrow beamwidth of the X-SAR inboard antenna. Fig. 6(a) shows the modeled X-SAR two-way inboard and outboard antenna pattern, as well as the effective pattern of the outboard antenna for an exact azimuth antenna beam alignment. In the case of a beam misalignment, as shown in Fig. 6(b), this superposition has the effect that a change in the azimuth angle of the outboard antenna, for example of $\Delta\theta_{az} = 0.2°$, transforms to an "electrically" measurable mainlobe peak displacement of the effective pattern of only $\Delta\theta_{az}^{elec} = 0.044°$. Since the measurement of the outboard Doppler centroid is related to the effective antenna pattern we need to distinguish between a mechanical or "steered" change
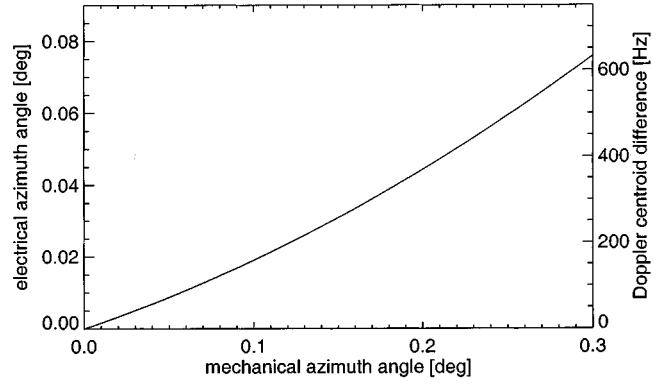

Fig. 7. Relationship between a mechanical or steered change in the antenna azimuth angle and the measurable effective beam misalignment, expressed as electrical azimuth angle or difference in Doppler centroid frequencies. The graph is referred to as "relaxing" curve.

in antenna azimuth angle and the resulting effective beam misalignment. By calculating the effective outboard pattern for different azimuth steering angles we derived the relation between the mechanical antenna azimuth angle and its effective "electrical" measurement. The resulting net effect on the difference in Doppler centroids was calculated using (5) and (13). The characteristic curve of this relation is plotted in Fig. 7. The relationship can be approximated by a straight line with a gradient of about $r_f = 0.24$ for the expected outboard antenna displacement range of $\pm 0.3°$. Hence, the factor r_f needs to be incorporated in (5) to derive the pitch and yaw angles for a mechanical rotation of the outboard antenna from Doppler centroid measurements, yielding

$$\Delta f_{DC} = f_{DC}^I - f_{DC}^O = \frac{2}{\lambda}|\vec{v}|r_f \cos\delta^I \sin\Delta\delta$$
$$= \frac{2}{\lambda}|\vec{v}|r_f \cos\delta^I(\theta_P \cos\vartheta_{el} - \theta_Y \sin\vartheta_{el}). \quad (14)$$

Similarly, for an electronic beam steering of the outboard antenna, estimation of the corresponding relative azimuth angle $\Delta\theta_{az}$ from Doppler centroid measurements also requires consideration of the factor r_f.

The effective diagram of the X-SAR outboard antenna has two different effects on the interferometric system performance, and hence on the azimuth antenna beam alignment requirement:

First, from (14) we can see that for a given pitch and yaw displacement of the outboard antenna, because of the factor $r_f = 0.24$ the resulting relative shift in Doppler frequency bands is significantly reduced. As a consequence, the X-SAR requirement on the antenna azimuth beam alignment can be relaxed. Therefore, r_f is called "relaxing" factor. This means, considering the requirement on the maximum allowable reduction in the interferogram azimuth bandwidth of $|\Delta f_{DC}^{\max}| = 300$ Hz (discussed in Section II), that the corresponding limit for the maximum difference in antenna azimuth angle can be raised from $|\Delta\theta_{az}^{\max}| = 0.036°$ to $|\Delta\theta_{az}^{\max - r_f}| = 0.15°$.

The effect of a reduced relative shift in Doppler frequency bands is typical for a single-pass SAR interferometer with one transmit/receive antenna and one receive-only antenna,
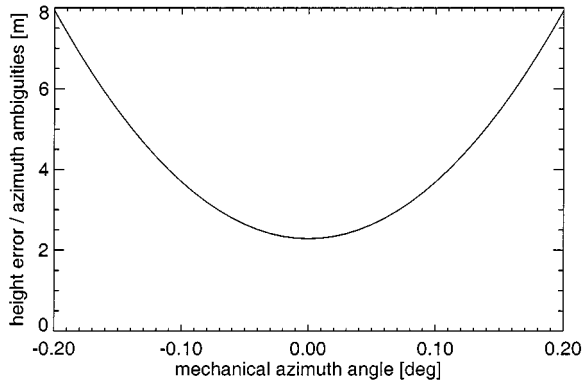
Fig. 8. Expected height error resulting from azimuth ambiguities for the effective X-SAR outboard antenna diagram as a function of the mechanical azimuth angle.

whereby r_f depends on the beamwidth of both antennas. However, even for a bistatic configuration with antennas of identical beamwidth, the "relaxing" factor would still be $r_f = 0.5$. In contrast, for a monostatic SAR interferometer configuration that uses the same antenna for transmit and receive, such as in the repeat-pass mode and the dual baseline "ping-pong" mode [17], it follows that $r_f = 1$.

In this context, it is interesting to note that in the case of a large inboard Doppler centroid caused by uncompensated shuttle attitude variations, the outboard Doppler centroid is shifted accordingly due to the rigid connection between the antennas. This along with an outboard antenna azimuth beam misalignment could cause the two Doppler centroid frequencies to be within different PRF bands. However, as discussed above, this additional shift of the outboard Doppler frequency band is minimized by the "relaxing" factor. Thus, for a sufficient zero-Doppler steering of the shuttle, the probability of having the inboard and outboard Doppler centroids in different PRF bands is significantly reduced. Otherwise, use of a Doppler ambiguity resolving algorithm [18], [19] is required, which, however, was restricted by performance requirements for the near real-time data analysis and the limited availability of two-channel radar data during the mission.

Second, depending on the difference in antenna azimuth angle, an increase in azimuth ambiguities is observed. This effect can be seen in Fig. 6(b). There is still a large overlap between the mainlobes of the inboard and the effective outboard antenna pattern, but the resulting high AASR for the effective pattern causes an increase in the interferogram phase noise, and hence an additional height error contribution. In Fig. 8, the expected height error due to azimuth ambiguities is plotted as a function of the mechanical antenna azimuth angle, based on (1) and (2). For the example discussed above with $\Delta\theta_{az} = 0.2°$, the AASR is about -7 dB, which corresponds to a height error of 10.3 m. Also, from this plot we can see that at the "relaxed" limit for the difference in antenna azimuth angle of $|\Delta\theta_{az}^{\max -r_f}| = 0.15°$, the additional height error is 5.8 m. However, this value exceeds the limit of $\sigma_h^{\max} = 4$ m that was specified for the maximum misalignment-induced height error in the overall X-SAR error budget. Consequently, the above-discussed "relaxed" requirement on the maximum allowable difference in antenna azimuth angle was tightened to

$|\Delta\theta_{az}^{\max -\text{limit}}| = 0.1°$, which causes a height error of 3.7 m. Note that a possible reduction of the phase noise in the interferogram by coherent "multilook" averaging is not considered here. Referring to Fig. 3, for this limit the resulting effective gain loss is -1.3 dB, causing a negligible signal decorrelation. Further, this maximum difference in azimuth angle is equivalent to a relative Doppler frequency band shift of about $|\Delta f_{DC}| = 200$ Hz. During the mission, the corresponding Doppler centroids were estimated with the sign Doppler estimator (SDE) [20]. The standard deviation of these estimates is about 1 Hz for the inboard channel, and about 5 Hz for the outboard channel, considering the above specified misalignment limit [21].

V. MISSION

A. Measurement Concept

Derivation of the milkstool "fine" adjustment solutions required the determination of the mechanical/electrical bias in AODA pitch and yaw estimates from measurements of the electrical boresight alignment between the inboard and outboard antenna. Thus, the respective Doppler centroid frequencies $\hat{f}_{DC}^I$, $\hat{f}_{DC}^O$ were estimated across the swath to provide the squint angle difference as a function of ϑ_{el} according to (14). Thereby, $\Delta\hat{\delta}_n$ denotes the estimated squint angle difference for the nth range bin with $n = 1, \ldots, N$, where $n = 1$ represents the near range and $n = N$ represents the far range. Using (8) with the approximation $\Delta\delta \cong \sin\Delta\delta$, the parametric model for the least square estimation (LSE) problem is given as

$$\Delta\hat{\delta}_n = \theta_P \cos\vartheta_{el}(n) - \theta_Y \sin\vartheta_{el}(n) + \varepsilon_n \quad \text{for } n = 1, \ldots, N$$

where ε_n stands for the superimposed noise due to measurement errors. Minimizing the squared error $S = \|\underline{\varepsilon}\|^2 = (\underline{\Delta\delta} - \underline{\underline{T}}\underline{\theta})^T(\underline{\Delta\delta} - \underline{\underline{T}}\underline{\theta}) = \min_\theta$ with

$$\underline{\underline{T}} = \begin{bmatrix} \cos\vartheta_{el}(1) & \sin\vartheta_{el}(1) \\ \vdots & \vdots \\ \cos\vartheta_{el}(N) & \sin\vartheta_{el}(N) \end{bmatrix},$$

$$\underline{\Delta\delta} = \begin{bmatrix} \Delta\delta_1 \\ \vdots \\ \Delta\delta_N \end{bmatrix}, \quad \text{and} \quad \underline{\theta} = \begin{bmatrix} \theta_P \\ \theta_Y \end{bmatrix}$$

yield the solution for the pitch and yaw estimates $\underline{\hat{\theta}} = (\underline{\underline{T}}^T\underline{\underline{T}})^{-1}\underline{\underline{T}}\underline{\Delta\delta}$.

The actual determination of the electrical boresight alignment was based on a joint analysis of C-RADAR and X-SAR Doppler centroid estimates to use their different measurement sensitivities to provide an optimal alignment solution for both radar systems. The large C-RADAR swath width (i.e., about five times as large as the X-SAR swath) enabled a more accurate estimation of the yaw angle due to $\theta_Y \sin\vartheta_{el}$ than was possible for X-SAR. However, according to (14), X-SAR provided about twice the sensitivity for the squint angle estimation from Doppler measurements than could be obtained with C-RADAR due to the difference in wavelength (i.e., assuming similar errors in Doppler

estimation). Consequently, determination of the electrical boresight alignment in pitch and yaw was performed in three steps:

Step 1) C-RADAR estimated $\hat{\theta}_Y$ across its four subswaths;

Step 2) X-SAR provided $\Delta\hat{\delta}_{X-SAR}(\vartheta_{el} = -7°)$ (at X-SAR midswath), considering the derived "relaxing" factor in (14);

Step 3) Both estimates were then used to calculate $\hat{\theta}_P$ taking into consideration (8) and $(\vartheta_{el} = -7°)$

$$\hat{\theta}_P = \frac{\Delta\hat{\delta}_{X-SAR}(\vartheta_{el}=-7°)}{\cos(\vartheta_{el}=-7°)} + \hat{\theta}_Y \tan(\vartheta_{el}=-7°).$$

These measurements enabled determination of the mechanical/electrical bias in AODA pitch and yaw alignment estimates, $\hat{\theta}_P^{AODA}$ and $\hat{\theta}_Y^{AODA}$, respectively, as follows:

$$\hat{\theta}_P^{bias} = \hat{\theta}_P^{AODA} - \hat{\theta}_P \quad \text{and} \quad \hat{\theta}_Y^{bias} = \hat{\theta}_Y^{AODA} - \hat{\theta}_Y.$$

This mechanical/electrical bias was then uploaded to the onboard AODA alignment estimation software to provide the crew with the "electrically" calibrated AODA alignment measurements for milkstool "fine" adjustment. Alternatively, for the correction of the residual misalignment by electronic antenna beam steering, the required azimuth angle can be calculated in (13) using either the pitch and yaw solutions as derived from Doppler centroid measurements or the calibrated AODA estimates.

B. Mission Results

After mast deployment and "coarse" milkstool adjustment based on the initial AODA observations, C-RADAR Doppler frequency measurements indicated a mechanical/electrical bias in pitch and yaw of $\hat{\theta}_P^{bias} = 0.1°$ and $\hat{\theta}_Y^{bias} = 0.121°$, respectively. In contrast, the results of the X-SAR Doppler frequency analysis showed only a negligible squint angle difference. Because of delays in the downlink of the high rate X-SAR data during the alignment analysis phase, the initial estimation of the mechanical/electrical bias was based entirely on C-RADAR measurements. The following pitch and yaw "fine" adjustments of the milkstool steered both outboard antennae more into flight direction (i.e., shuttle tail). Whereas the C-RADAR beams were then aligned, the X-SAR beams became misaligned because of the milkstool adjustments. As a consequence, X-SAR compensated for the resulting misalignment by electronic azimuth beam steering of its outboard antenna by $\Delta\theta_{az} = 0.085°$ (nearest beam steering step) in direction to the shuttle's nose (i.e., opposite to the direction of the prior milkstool rotation). Fig. 9 illustrates the steps conducted during the initial phase of the antenna beam alignment. Ground receiver measurements of the C-RADAR and X-SAR inboard antenna beams, taken at DLR's calibration test site (see Fig. 10), indicated that the discrepancy in the alignment results between the two radar systems could be attributed to an offset between the C-RADAR and X-SAR inboard antenna beams. As shown in Fig. 10, the peak of the X-SAR beam is delayed by 0.1 s with respect to the peak of the C-RADAR beam. This is equivalent to a difference in azimuth angle between the two inboard beams of about 0.1°.

The electrical beam alignment was analyzed and verified throughout the mission whenever down linked two-channel
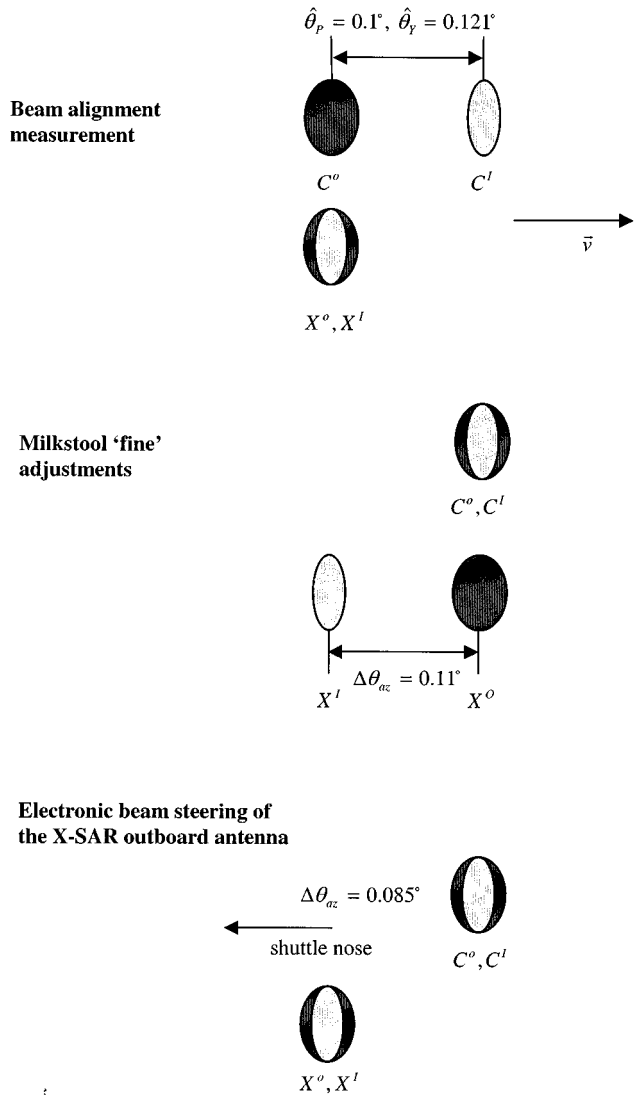

Fig. 9. Illustration of the steps during the initial phase of the antenna beam alignment in azimuth.
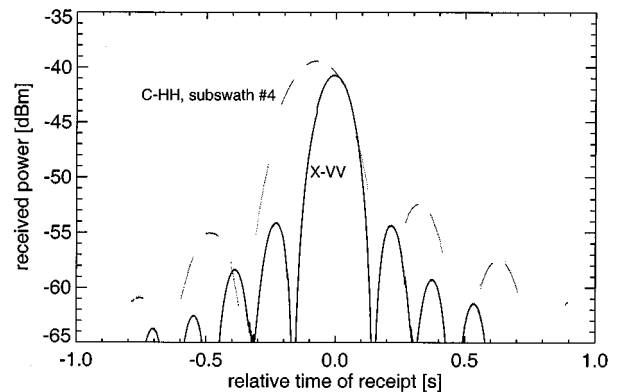

Fig. 10. Ground receiver measurements of the C-RADAR and X-SAR inboard antenna beams. The gaps in the C-RADAR curve are due to the ScanSAR burst mode.

X-SAR data was available, covering usually a time frame of 1–2 min of the mission elapse time (MET). To allow tracking of the inboard and outboard Doppler centroids along azimuth, these estimates were updated every second. The variation of the Doppler centroids across the swath was determined by
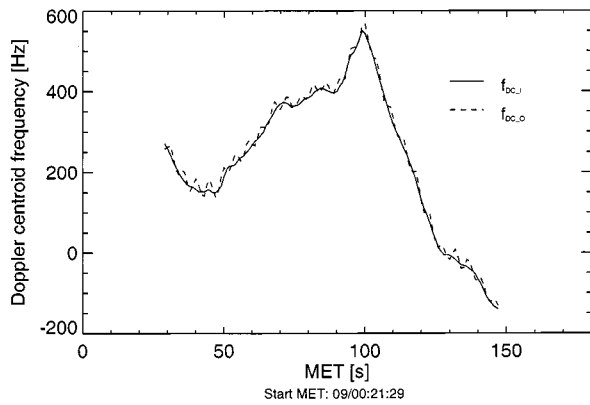
(a)
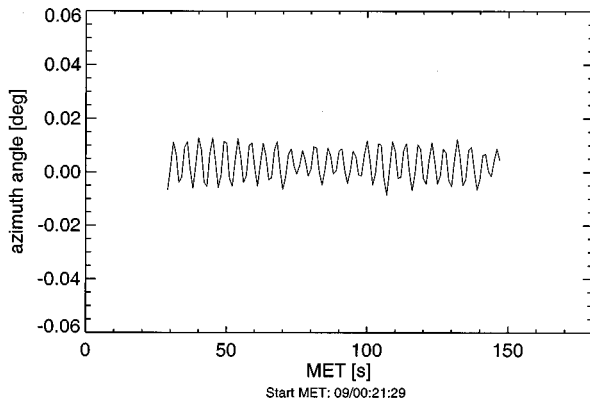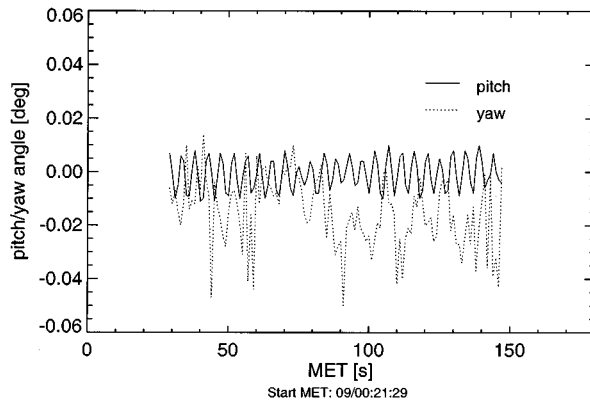
(b)

Fig. 11. (a) Doppler centroid frequencies of the inboard and outboard channel for an ocean datatake. (b) Alignment analysis results: pitch and yaw displacements of the outboard antenna (top), and the resulting mechanical azimuth angle (bottom).

analyzing eleven independent segments, each averaged over 302 range bins [21]. In Fig. 11(a), for an ocean datatake, the X-SAR inboard and outboard Doppler centroid frequencies are plotted versus MET. For this representative example, the mean offset between the two curves is only about 6 Hz, causing a negligible reduction in the interferogram azimuth bandwidth, and hence spatial resolution. Fig. 11(b) shows the derived pitch and yaw displacements of the outboard antenna (top), and the resulting mechanical antenna azimuth angle (bottom), respectively. It can be seen that the pitch angle was relatively constant
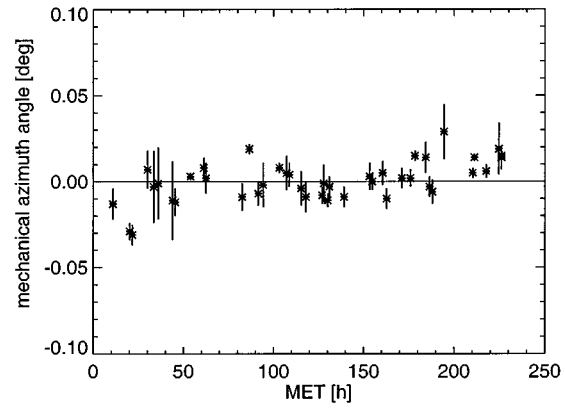

Fig. 12. Plot of the X-SAR mechanical azimuth angle difference including its error bar as estimated throughout the mission versus MET.

while the yaw angle slightly oscillates, possibly caused by mast bending. Based on alignment results obtained during the mission from the analysis of down linked two-channel X-SAR data, we show in Fig. 12 a plot of the mechanical antenna azimuth angle including its error bar, covering the complete data acquisition time frame of the mission's mapping phase. Unexpectedly, the mechanical azimuth angle of the X-SAR outboard antenna remained relatively stable with $|\Delta\theta_{az}| \leq 0.05°$. This is significantly below the specified requirement of $|\Delta\theta_{az}^{\max\_\text{limit}}| = 0.1°$. As a result, the X-SAR electronic azimuth beam steering offset was kept constant throughout the mission after the initial antenna beam alignment.

VI. CONCLUSIONS

In this paper, we considered the on-orbit interferometric X-SAR antenna beam alignment during the SRTM/X-SAR mission. Antenna beam alignment is essential for achieving best interferometric performance, including spatial resolution and height accuracy. We discussed the effects of beam misalignment on the interferometric phase noise, considering specifically the SNR, the relative shift of the Doppler frequency bands, and the AASR. We showed that in elevation the effective antenna gain loss due to roll misalignment is negligible. Since the alignment sensitivity in azimuth is an order of magnitude higher than in range, we concentrated therefore on the azimuth beam alignment. For a cross-track SAR interferometer configuration with one transmit/receive antenna and one receive-only antenna we established the relation between pitch and yaw displacements of the outboard antenna beam and the relative shift of the inboard and outboard Doppler frequency bands. The corresponding Doppler measurements were used to determine the mechanical/electrical bias in the AODA alignment estimates. They also provided the solutions for mechanical milkstool adjustments and electronic beam steering of the outboard antenna to correct for azimuth beam misalignment. The analysis of the effects of the effective X-SAR outboard antenna pattern revealed that for an accurate alignment determination we need to distinguish between a mechanical or "steered" change in antenna azimuth angle and the effective, electrical beam misalignment. The corresponding relationship is linear for the expected outboard antenna displacement range, and a so-called "relaxing" factor

was determined. As a result, on one hand, the limit for the difference in antenna azimuth angle could be increased by a factor of $1/r_f = 4.17$, considering the maximum allowable relative shift of the Doppler frequency bands. On the other hand, we showed that in the case of an azimuth beam misalignment the resulting high AASR for the effective antenna pattern causes an additional height error. Hence, the "relaxed" limit for the relative antenna azimuth angle had to be reduced to minimize this height error contribution. The alignment results obtained throughout the mission from calibrated AODA and Doppler centroid frequency measurements showed that the maximum difference between the X-SAR inboard and outboard antenna azimuth angles was below the specified limit by a factor of two. This can be attributed to lower than expected dynamic mast twisting and bending motions.

The geometrical considerations to derive from Doppler frequency measurements accurate solutions for correcting beam misalignment, and the described effects of the antenna diagrams on the alignment requirement may be useful for the design and operations of future satellite SAR interferometry missions, especially for those that will use a bistatic interferometer configuration.

ACKNOWLEDGMENT

REFERENCES

[1] E. R. Stofan, D. L. Evans, Ch. Schmullius, B. Holt, J. J. Plaut, J. van Zyl, S. D. Wall, and J. Way, "Overview of results of spaceborne imaging radar-C, X-band synthetic aperture radar (SIR-C/X-SAR)," *IEEE Trans. Geosci. Remote Sensing*, vol. 33, pp. 817–828, July 1995.
[2] R. L. Jordan, B. L. Huneycutt, and M. Werner, "The SIR-C/X-SAR synthetic aperture radar system," *IEEE Trans. Geosci. Remote Sensing*, vol. 33, pp. 829–839, July 1995.
[3] J. Moreira, M. Schwäbisch, G. Fornaro, R. Lanari, R. Bamler, D. Just, U. Steinbrecher, H. Breit, M. Eineder, G. Franceschetti, D. Geudtner, and H. Rinkel, "X-SAR interferometry: First results," *IEEE Trans. Geosci. Remote Sensing*, vol. 33, pp. 950–956, July 1995.
[4] R. Duren, E. Wong, B. Breckenridge, S. Shaffer, C. Duncan, E. Tubbs, and Ph. Salomon, "Metrology, attitude, and orbit determination for spaceborne interferometric synthetic aperture radar," *Proc. SPIE*, vol. 3965, pp. 51–60, Apr. 1998.
[5] R. Duren, "Attitude and orbit determination avionics (AODA) functional requirements document," Jet Propulsion Laboratory, California Institute of Technology, Pasadena, CA, Tech. Note, Feb. 1999.
[6] M. Werner, "Shuttle radar topography mission (SRTM)," in *Proc. 3rd EUSAR*, Munich, Germany, May 2000, pp. 209–212.
[7] E. Rodriguez and J. M. Martin, "Theory and design of interferometric synthetic aperture radars," *Proc. Inst. Electr. Eng.*, pt. F, vol. 139, no. 2, pp. 147–159, 1992.
[8] H. A. Zebker and J. Villasenor, "Decorrelation in interferometric radar echoes," *IEEE Trans. Geosci. Remote Sensing*, vol. 30, pp. 950–959, Sept. 1992.
[9] D. Just and R. Bamler, "Phase statistics of interferograms with applications to synthetic aperture radar," *Appl. Opt.*, vol. 33, no. 20, pp. 4361–4368, 1994.
[10] M. Schwäbisch and D. Geudtner, "Improvement of phase and coherence map quality using azimuth prefiltering: Examples from ERS-1 and X-SAR," in *Proc. IGARSS*, Florence, Italy, 1995, pp. 205–207.
[11] D. Geudtner and M. Zink, "Interferometric calibration of the X-SAR system on the shuttle radar topography mission (SRTM/X-SAR)," in *Proc. 21th Canadian Remote Sensing Symp.*, Ottawa, ON, Canada, June 1999, pp. 558–565.
[12] J. C. Curlander and R. N. McDonough, *Synthetic Aperture Radar, Systems and Signal Processing*. New York: Wiley, 1991, Wiley Series in Remote Sensing.
[13] R. B. Dybdal and R. H. Ott, "Coherent RF error statistics," *IEEE Trans. Microwave Theory Tech.*, vol. MTT-34, pp. 1413–1419, Dec. 1986.
[14] K. B. Klein and R. L. Jordan, "X-SAR/SRTM: performance parameter definition document," DLR-JPL, Tech. Rep., 1998.
[15] C. Wu, J. C. Curlander, and A. di Cenzo, "Determination of spacecraft attitude using synthetic aperture radar data," *Proc. AIAA*, pp. 57–60, 1980.
[16] K. Eldhuset, "Accurate attitude estimation using ERS-1 SAR raw data," *Int. J. Remote Sens.*, vol. 17, no. 14, pp. 1827–1844, 1996.
[17] P. A. Rosen, S. Hensley, I. R. Joughin, F. K. Li, S. N. Madsen, E. Rodriguez, and R. M. Goldstein, "Synthetic aperture radar interferometry," *Proc. EEE*, vol. 88, pp. 333–382, Mar. 2000.
[18] R. Bamler and H. Runge, "PRF-ambiguity resolving by wavelength diversity," *IEEE Trans. Geoscience Remote Sensing*, vol. 29, pp. 997–1003, Nov. 1991.
[19] F. Wong and I. G. Cumming, "A combined SAR Doppler centroid estimation scheme based upon signal phase," *IEEE Trans. Geosci. Remote Sensing*, vol. 34, pp. 696–707, May 1996.
[20] S. N. Madsen, "Estimating the Doppler centroid of SAR data," *IEEE Trans. Aerosp. Electron. Syst.*, vol. 25, pp. 134–140, Mar. 1989.
[21] S. Buckreuss, R. Scheiber, and C. Basler, "The X-SAR/SRTM radar data analyzer," in *Proc. 3rd EUSAR*, Munich, Germany, May 2000, pp. 219–221.

Dirk Geudtner received the M.Sc. degree in geophysics from the Technical University "Mining Academy" Freiberg, Germany, in 1991, and the Ph.D. degree from the Institute of Navigation, University of Stuttgart, Germany, in 1995.

He joined the German Aerospace Center (DLR) in 1991, where he worked on ERS SAR interferometry processing. From 1994 to 1995, he joined the GeoForschungsZentrum (GeoResearch Center) Potsdam (GFZ), where he was responsible for the geoscientific application of SAR interferometry. Between 1995 and 1997, he was a Visiting Scientist at the Canada Centre for Remote Sensing (CCRS) working on differential ERS-1/2 SAR interferometry studies. In 1997, he joined the Institute of Radio Frequency Technology at DLR, where he developed calibration/validation concepts for the X-SAR system on the Shuttle Radar Topography Mission (SRTM/X-SAR). For SRTM/X-SAR, he was the lead engineer for the X-SAR interferometry analysis at the Payload Operations Control Center in Houston. While holding a research grant from the Humboldt-Foundation, he has been working since July 2000 as a Visiting Scientist at CCRS on interferometric processing of RADARSAT SAR data for mapping of terrain movement and on aspects related to polarimetric calibration.

Manfred Zink received the Dipl.-Ing. degree in physics from the Technical University of Graz in 1987 and the Dr.-Ing. degree from the University of Stuttgart in 1993. In 1988, he joined the Microwave and Radar Institute at the German Aerospace Center. He has pioneered calibration techniques for both airborne and spaceborne SAR sensors and was responsible for building up the Oberpfaffenhofen calibration site. He was the Lead X-SAR Calibration Engineer for both SIR-C/X-SAR missions in 1994 and for the SRTM mission in 2000. In August 2000, he joined the European Space Agency, where he is responsible for the Calibration/Validation of the Advanced Synthetic Aperture Radar (ASAR) onboard the ENVISAT satellite.

Christoph Gierull (S'94–M'95) received the Dipl.-Ing. and the Dr.-Ing. degrees in electrical engineering from the Ruhr-University Bochum, Germany, in 1990 and 1995, respectively. From 1991 to 1994, he was a scientist at the Electronics Department of the German Defence Research Establishment (FGAN) in Wachtberg. From 1994 to 1999, he was the head of the SAR-simulation group at the Institute of Radio Frequency Technology at the German Aerospace Center (DLR) in Oberpfaffenhofen. He received the 1998 paper prize award of the Information Technology Society (ITG) of the Association of German Electrical Engineers (VDE). In 2000, Dr. Gierull joined the Aerospace Radar and Navigation Section at Defence Research & Development Canada - Ottawa (DRDC-O) as a Defence Scientist. In Feb. 2000, he was a X-SAR performance engineer on the Shuttle Radar Topography Mission's operations team at the Johnson Space Centre in Houston, TX. His interests include all aspects of radar (array) signal processing, including adaptive jammer suppression, superresolution, space-time adaptive processing, and synthetic aperture radar techniques in combination with MTI.

Scott Shaffer received the B.S. and M.S. degrees in electrical engineering from the University of California, Berkeley, in 1984 and 1986, respectively.

Since joining the Jet Propulsion Laboratory, California Institute of Technology, Pasadena, he has worked on a variety of airborne and spaceborne radars. Currently, he is the cognizant engineer for the Mars Exploration Rover (MER) landing altimeter. Previous tasks have included system engineering for the Shuttle Radar Topography Mission (SRTM), qualification and testing of the Mars Pathfinder landing altimeter, performance analysis and verification of the Spaceborne Imaging Radar-C (SIR-C), demonstrations of stereo and interferometric height determination using Magellan radar data, and wind retrieval algorithm assessment for the NASA Scatterometer (NSCAT).